Interface-induced effects on the polarization response of epitaxial ferroelectric thin films—an experimental study and theoretical analysis

6

Evert P. Houwman, Luuk Okkerman, Minh T. Do, Gertjan Koster and Guus Rijnders
Inorganic Material Science, MESA+ Institute for Nanotechnology, University of Twente, Enschede, The Netherlands

1. Introduction

Ferroelectric thin films are of much interest for many applications (Setter and Damjanovic, 2006). One can divide the field roughly into that of ferroelectric thin films (few 100 nm and less) and very thin devices (few nm's) on the one side and that of "thick" thin films (from 500 nm up to micrometers) on the other hand. The latter group is mainly used for mechanical applications, employing the direct or indirect piezoelectric effect. The research on thin film devices has for a long time been focused on ferroelectric memory applications, in which the polarization direction is used as the "0" or "1" bit and more recently on ferroelectric tunnel junctions, in which the ferroelectric layer functions as tunnel barrier with switchable or tunable tunnel probability between a low and a high value in multiple steps or even on a more or less continuous scale (Ishiwara, 2012; Auciello et al., 2014; Garcia and Bibes, 2014; Wen and Wu, 2020). The tunnel junction may also be used in resistive memory or neuromorphic applications (Kim et al., 2012; Ma et al., 2020; Mikheev et al., 2020). There is also much interest in the mechanical properties employed in sensors, actuators, and transducers, often in Si-based MEMS devices (Tadigadapa and Mateti, 2009; Koh et al., 2011; Eom and Trolier-McKinstry, 2012; Funakubo et al., 2012; Priya et al., 2017; Isarakorn et al., 2010; Vu et al., 2015; Nguyen et al., 2016a, 2017a,b), for which one mostly needs thicker films to generate sufficient signal (induced charge or voltage) or force (mostly bending of substrate by in-plane stress), but sometimes also a piston motion for accurate vertical displacements (Nematollahi et al., 2019).

It has been recognized early on that in thin-film devices the interfaces play an important role in the ferroelectric and piezoelectric performance and fatigue behavior of devices. The effect of a thin dielectric layer (of undefined origin) at the ferroelectric−electrode interface on the polarization loop has been studied extensively

Epitaxial Growth of Complex Metal Oxides. https://doi.org/10.1016/B978-0-08-102945-9.00001-0
Copyright © 2022 Elsevier Ltd. All rights reserved.

theoretically and was in 2006 summarized in an extensive review paper (Tagantsev and Gerra, 2006). The models and the then existing body of experimental data provide a solid base for the interpretation of new data. In the same year, it was suggested that the dielectric interfacial layer can be an important cause of polarization fatigue by strongly enhancing local charge injection current densities, leading to local phase decomposition (Lou et al., 2006, 2007; Lou, 2009). One can find in the more recent literature since the 2006-publications little about interface-induced effects. The papers (Tagantsev and Gerra, 2006; Lou et al., 2006, 2007; Lou, 2009) have regularly been used as reference for qualitative explanations of observed polarization or fatigue behavior, but to the best of our knowledge, detailed studies on interface-related effects are lacking, despite the relevance for many applications of ferroelectric thin films. Recent work (Do, 2021; Do et al., 2020, 2021) in our group on polarization fatigue of devices based on $Pb(Zr_{1-x}Ti_x)O_3$ (shorthand PZT, and mainly with the Morphotropic Phase Boundary composition, $x = 0.48$) showed in great experimental detail that the charge injection mechanism, as suggested in ref. Lou et al. (2006, 2007), Lou (2009), is applicable under certain conditions.

Since the start of our investigations, in about 2006, into the growth and properties of high quality (epitaxial) ferroelectric thin films, manufactured by pulsed laser deposition (PLD), and deposited on various substrates and employing different buffer or seed layers, we have observed in many of our devices changes in the polarization hysteresis loop (PE-loop) that can be related to the interfaces of the ferroelectric layer with the electrodes. In this chapter, we present a detailed experimental study of several simultaneously occurring effects arising from the bottom-electrode—ferroelectric interface in epitaxial thin film PZT capacitor devices fabricated in our laboratory.

We consider epitaxial PZT capacitor devices, grown on a perovskite substrate (usually $SrTiO_3$ (STO)) and with the same conducting oxide top and bottom electrodes (mostly $SrRuO_3$ (SRO)) as the most ideal devices we can obtain experimentally. The ferroelectric and piezoelectric properties hardly change with cycling (no fatigue) and one would expect that the properties can be attributed to the ferroelectric layer only. However, it appears that even in the best devices, the interfaces can have a significant effect on the performance of all-oxide ferroelectric devices due to extrinsic effects: the polarization-hysteresis loop (PE-loop), and even the fatigue properties, may change depending on the ferroelectric layer thickness and electrode material used. In our lab, we use SRO/PZT/SRO-on-(001)-oriented-STO devices as benchmark for the properties of devices grown with different materials (different PZT compositions, without or without doping (Nguyen et al., 2014), different ferroelectric materials (Boota et al., 2014, 2016; Nguyen et al., 2016b), substrates (Nguyen et al., 2011, 2017c; Dekkers et al., 2009; Li et al., 2018, 2020), and electrode materials (Wang et al., 2020). Therefore it is important to have a good understanding of the effect of the SRO electrode layer and the SRO/PZT interfaces.

In Section 2, we analyze the experimental results on epitaxially grown SRO/PZT/SRO-on (001)-oriented STO devices and relate the ferroelectric properties to the crystalline structure of the bottom electrode—ferroelectric interface. In Section 3, the results are interpreted in terms of some of the long-standing models discussed in literature.

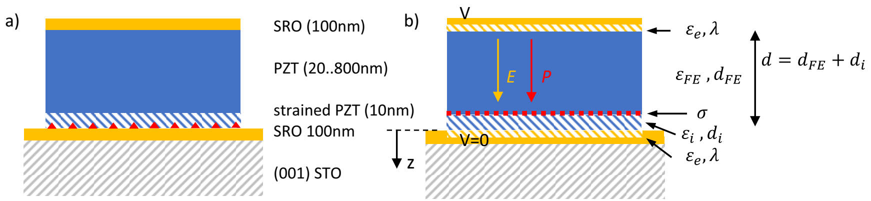

Figure 6.1 (A) Schematic cross-section of an epitaxial SRO/PZT/SRO capacitor on (001)STO, showing the strained interfacial layer with the equidistant line defects at the bottom electrode−ferroelectric interface (red triangles). (B) Model of the capacitor stack, defining the ferroelectric, charged, passive layer, and screening layers and the associated parameters.

2. Model interface structure and sample description

Here we focus on the interface of the bottom SRO electrode with a $PbZr_{0.52}Ti_{0.48}O_3$ (short PZT) ferroelectric layer in a SRO/PZT/SRO capacitor stack on a (001)-oriented, single-terminated STO substrate, with single unit cell step heights between the TiO_2-terminated terraces. SRO grows cube-on-cube on the STO and is fully (in-plane compressively) strained to the substrate up to the thickness (here 100 nm) of the bottom electrode. The PZT starts to grow cube-on-cube on the SRO, but due to the large lattice mismatch between STO/SRO and PZT, it is strongly compressively strained and on regular distances line defects develop in the PZT close to the SRO/PZT interface (see Fig. 6.2B), which relax the strain within a layer thickness of the order of 10 nm (Boota et al., 2014). Near the lattice defects one observes the surrounding strain field in the PZT and SRO and the relaxation of the local deformations of the film. Simplifying the description of the strain field to one dimension by averaging out the lateral spatial variation of the strain field, one can describe the strain in the bottom part of the PZT layer by equal gradients of the in-plane strain components in the out-of-plane (z-) direction ($\partial\varepsilon_{xx}/\partial z = \partial\varepsilon_{yy}/\partial z$) and the out-of-plane strain gradient ($\partial\varepsilon_{zz}/\partial z$), with $\boldsymbol{\varepsilon}(z)$ the in-plane averaged strain vector field as function of z position. In this chapter, it is shown that this interfacial strain-gradient layer can explain the changes in ferroelectric properties of devices as function of the PZT-layer thickness.

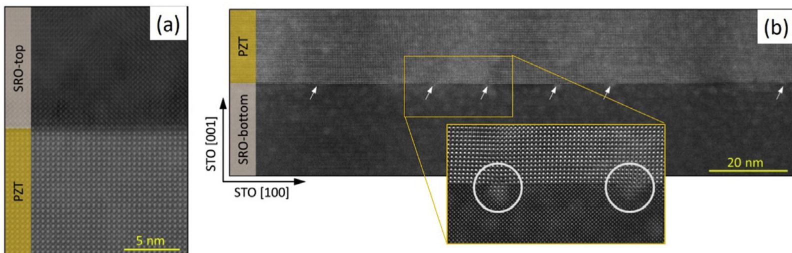

Figure 6.2 Transmission electron microscopy investigation of the top (A) and bottom SRO/PZT interface (B) showing heteroepitaxial growth of the different layers and the strain fields in the SRO and PZT around the line defects (indicated by the *arrows*).

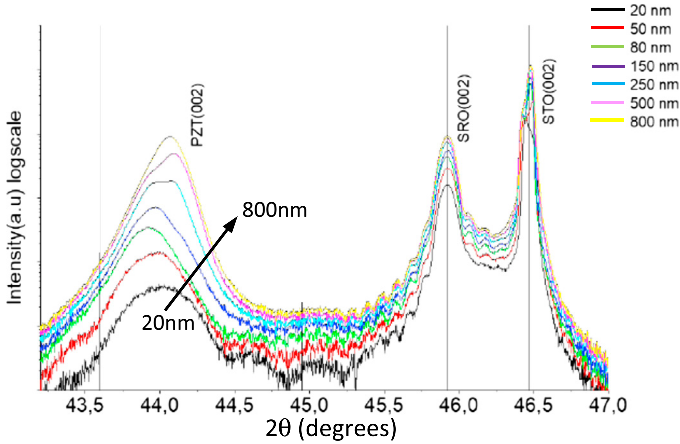

Figure 6.3 X-ray Diffraction of SRO/PZT/SRO stacks on (001)-STO for different PZT thicknesses.

Apart from the initial strain-gradient layer and the line defects at the bottom interface, the PZT layer grows largely defect free up to the top electrode (Fig. 6.2). The top surface of the PZT has sub-nm roughness, as was measured with AFM on layer stacks without top electrode. Fig. 6.2A also shows that the PZT/SRO top interface is nearly atomically sharp. It is noted that the 100 nm SRO top electrode grows (001)-oriented, but in a polycrystalline way, which is attributed to the large lattice mismatch of SRO grown on PZT, creating a large nucleation density.

X-ray diffraction (Fig. 6.3) of the capacitor stacks with increasing PZT thickness shows a change in the width and peak position of the PZT(002) reflection, which reflects the change in strain state of the PZT-layer. With increasing thickness, the average out-of-plane lattice parameter decreases, hence the initially compressed in-plane parameter relaxes from the epitaxially strained value (imposed by the cube-on-cube growth) to the thermally strained value (imposed by thermal mismatch between substrate and film). The indicated SRO(002) peak is that of the bottom electrode and its position can be shown to be due to epitaxial strain to the substrate. The SRO top electrode reflection is smeared out between those of the SRO bottom electrode and the STO, indicating a strain distribution in this polycrystalline layer.

3. Effects of SRO/PZT interface on ferroelectric properties

In ref. Tagantsev and Gerra (2006), it is shown that there are several effects of a (possibly polar and/or charged) dielectric layer (also often named the “passive” layer, thickness d_i) that may be present at the interface of the electrode and the ferroelectric layer (thickness d_{FE}). The total thickness of the ferroelectric and dielectric layers is $d = d_{FE} + d_i$. Fig. 6.1 shows schematically the investigated structure. It is assumed

that there is a passive layer at the bottom interface, between the bottom SRO electrode and the ferroelectric, of which we will investigate quantitatively the properties. Since there are no experimental indications of the contrary, no such layer is assumed to be present at the top SRO electrode. The SRO electrodes have a high, but finite electron density and conductivity and thus a finite screening length.

The bottom electrode is assumed to be grounded—as is always the case in our experiments—so that a positive electric field value corresponds to a top-to-bottom–oriented field vector and a positive voltage V on the top electrode. Note that this can be different in other literature, which can give rise to different signs (i.e., directions) of electric field and polarization vectors. This can be very confusing when using formulas, based on the wrong polarity definition.

In the following sections, we discuss the difference in polarization hysteresis loops, specifically of the slanting, the coercive field, and the self-bias field, of a series of SRO/PZT/SRO/(001)STO capacitor devices. In this series, the only parameter that is intentionally changed is the thickness d of the PZT layer, which is varied between 25 and 800 nm. The effect on the PE-loop is analyzed in detail and we will show that for the thinner samples, the effect of the strain-gradient layer on the PE-loop is large, while this effect decreases with increasing thickness. Further the properties of the strain gradient layer are determined. Section 3.1 describes the effect on slanting of the loop of a series dielectric layer in the ferroelectric capacitor stack. In Section 3.2 we explain in detail how one can—under certain conditions—analyze the experimental coercive field values to separate the change of the intrinsic self-bias field from the possible simultaneous change of intrinsic coercive fields with FE-layer thickness. In Section 3.3 the change of the coercive field due to a dielectric layer is described. The model is used to analyze the extracted measured coercive field data. In the case of a capacitor with electrodes with the same work function, the thickness-dependent self-bias field can be attributed to an effective charge (Section 3.4). This charge can have several causes: trapped charge (arising from defects and injected and subsequently trapped electrons) and a fixed polarization charge and its associated field arising from the flexoelectric effect (Section 3.5).

3.1 Slanting of the or thin FE-layers

Fig. 6.4A shows the polarization (PE) hysteresis loops of several devices from the investigated series, with varying thickness of the FE-layer. The most obvious difference between the loops is the increasing slanting with decreasing PZT thickness. This can straightforwardly be shown to be the consequence of the presence of a dielectric layer in the device (Tagantsev and Gerra, 2006).

Consider a one-dimensional model of the structure as shown in Fig. 6.1B. The describing equations are obtained from the continuity of the normal component of the dielectric displacement across the various interfaces and the total voltage drop, V, across the device:

$$\varepsilon_0 \varepsilon_e E_b = \varepsilon_0 \varepsilon_i E_i \tag{6.1a}$$

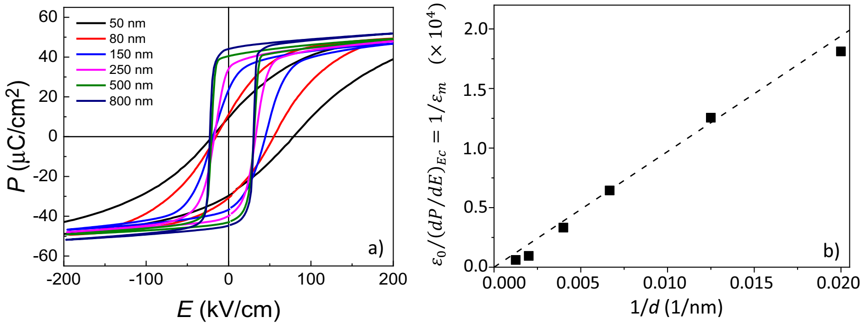

Figure 6.4 (A) Increased slanting of the polarization hysteresis loops of SRO/PZT/SRO-on-(001)STO substrates with decreasing PZT thickness. (B) Inverse of the slope (Eq. 6.5) of the PE-loop at the coercive field as function of the inverse of PZT thickness.

$$\varepsilon_0 \varepsilon_i E_i = \varepsilon_0 E_{FE} + P_z(E_{FE}) \tag{6.1b}$$

$$\varepsilon_0 E_{FE} + P_z(E_{FE}) = \varepsilon_0 \varepsilon_e E_t \tag{6.1c}$$

$$\lambda E_b + d_i E_i + d_{FE} E_{FE} + \lambda E_t = d E_m = V \tag{6.2}$$

Here, λ, ε_e, and ε_i are the screening length and in the electrodes relative dielectric constant of the screening layers in the electrodes and of the passive layer, respectively. E_b, E_t, and E_i are the fields in the bottom and top screening layers and the dielectric layer, respectively. $P_z(E_{FE})$, E_{FE} are the field-dependent z-component of the polarization and the local field in the ferroelectric layer, while E_m is the "measured" field, as is calculated from the voltage drop across the device, with "measured" (i.e., deposited) film thickness d. The z-component of the displacement in the ferroelectric can well be approximated by the polarization, $D_{z,FE} = \varepsilon_0 E_{FE} + P_z \approx P_z$. For simplicity, we assume that the polarization is of the order of the measured saturation polarization, P_s. From the above equations, one arrives at:[1]

$$E_{FE} = \frac{d}{d_{FE}} E_m - \left(\frac{d_i}{d_{FE} \varepsilon_i} + \frac{2\lambda}{d_{FE} \varepsilon_e} \right) \frac{P_z(E_{FE})}{\varepsilon_0} \tag{6.3}$$

$$E_i \approx \frac{P_s}{\varepsilon_0 \varepsilon_i} \quad , \quad E_b = E_t \approx \frac{P_s}{\varepsilon_0 \varepsilon_e} \tag{6.4}$$

From Eq. (6.3) it is seen that only for thick films the field seen by the ferroelectric is approximately equal to the external (measured) field E_m, because then $d_{FE} \approx d$ and the

[1] In this derivation, we have assumed that the PE-loop is driven to high enough fields E_{max}, so that the shape of the loop is not dependent on the maximum field. In ref. Tagantsev and Gerra (2006), the authors also consider the change of the shape of the loops due to unsaturated PE-loop cycling, but that is outside the scope of this study.

bracketed term becomes negligibly small. Thus one expects to see only effects arising from the dielectric and/or screening layers for small film thicknesses. Further it is noted that the above derivation, and therefore also the results with respect to the slanting, discussed below, do not depend on the position of the dielectric layer, i.e., if it is at the top or at the bottom electrode interface. Eq. (6.4) indicates that the electric fields across the dielectric layer and the screening layers can be extremely large (of the order of 10's MV/cm).[2] Taking the derivative of Eq. (6.3) with respect to the polarization P_z, one finds for the inverse of the slope of the measured loop at the coercive field, $1/\varepsilon_0\varepsilon_m \equiv (dP_z/dE_m)^{-1}_{E_c}$ the relation:[3]

$$\frac{1}{\varepsilon_m} = \frac{1}{d}\left(\frac{d_i}{\varepsilon_i} + \frac{2\lambda}{\varepsilon_e} + \frac{d_{FE}}{\varepsilon_{FE,Ec}}\right) \tag{6.5}$$

Here $\varepsilon_0\varepsilon_{FE,Ec} = (dP_z/dE_{FE})_{Ec}$ is the slope of the measured loop of an ideal FE device at the coercive field, not affected by interfacial effects. $\varepsilon_0\varepsilon_{FE,Ec}$ is a good approximated by the slope at large thicknesses, when $d_{FE} \approx d$. For a "square" loop with abrupt switching from the up to the downward polarization state and vice versa, as is observed for the device with $d = 800$ nm in Fig. 6.4A, it is seen that $\varepsilon_{FE,Ec}$ » 1. The slope of the $1/\varepsilon_m$−versus−d plot provides a value for the bracketed term in Eq. (6.5). The effect of the electrode screening effects is *not* a priori neglected, since for large ε_i, the remaining two terms inside the brackets might be of comparable size.

For the discussed SRO/PZT system, the thickness-dependent PE-loop canting is observed. It is concluded (i) that there is a nonswitchable, dielectric layer present and (ii) the intrinsic loop is nearly square (hence $\varepsilon_{FE,Ec} \to \infty$). The bracket term in Eq.(6.5) is found to be approximately equal to 0.1 Å. (iii) The fact that the offset of the curve is zero also implies that there is little to no spread in the value of the coercive field at different positions across the area of the various devices or said differently that there is just a single coercive field. Such spread would provide an additional cause for canting.

[2] The electric fields across the dielectric layer and the screening layers can be extremely large, depending on the values of the dielectric constants of these layers (of the order of 10's MV/cm). Such fields may cause (electronic) charge injection into the ferroelectric (depending on the direction of the polarization or field driven ion diffusion, and in this way changes of the electrical properties of the device (fatigue) (Lou et al., 2006, 2007; Lou, 2009; Do, 2021; Do et al., 2020, 2021).

[3] Eq.(6.5) has been derived without taking the limit $d \gg d_i$ as is done in Eq.(2.6) in Tagantsev and Gerra (2006), which there results in an nonzero offset term $1/\varepsilon_{FE,Ec}$. This allows the authors to describe the experimental results on sol−gel derived films in fig. 3 in that reference, which cannot be done without taking this limit. It appears to us that the large offset in the data in fig. 3 cannot be explained by the intrinsic slope $\varepsilon_{FE,Ec}$ of the PE-loop. We suggest that the investigated devices show a significant spread in coercive field values across the device area, which may account for the offset of the curve in fig. 3. Further we note that our data extend over a much larger $1/d$ range, namely from $d = 50$ nm upwards, as compared to $d =$ 140 nm and larger in Tagantsev and Gerra (2006). Thus our data provide a more rigorous proof of the interfacial layer model causing canting of the PE-loop.

3.2 Disentangling self-bias field and coercive field changes

Fig. 6.5A shows the positive and negative coercive field of the various devices. Two trends are visible: (i) an increase of the positive measured coercive field, E^+_{cm}, with decreasing thickness, and a (nearly) thickness independent value of the negative coercive field, E^-_{cm}; (ii) an increasing loop opening $\Delta E_c = E^+_{cm} - E^-_{cm}$ with decreasing d. This suggests that simultaneously there are two different mechanisms at play. If only a possibly present self-bias field would change with thickness, then ΔE_c would remain constant for varying film thickness and the coercive fields would be offset with a thickness-dependent internal self-bias field. However, since also the loop opening changes we conclude that also the coercive fields vary with thickness.

To analyze this in more detail, we make the assumption that the polarization switching arises from nucleation of reverse polarization domains at the electrode interfaces and not in the bulk of the ferroelectric (Tagantsev and Gerra, 2006). In this nucleation-limited switching model, the nucleated reverse domains become stable and can grow when the applied field is so large that the energy gain associated with the domain polarization is larger than the energy cost for the creation of the domain walls of the reverse domain. This critical field value can be identified with the coercive field. After nucleation, which we regard as the limiting step in the polarization reversal process in the high quality, epitaxial films considered here, the domain walls between the forward and reverse domains rapidly move in forward and sideway direction, completing the reversal. This is a widely accepted picture of polarization reversal in literature. What has not been so clearly discussed and understood is the question if the reversal domains nucleate simultaneously at both electrode interfaces, at only one interface, or at different interfaces for, respectively, the positive and negative coercive field. On the basis of experiments with devices with electrodes made from different materials, we conclude that—at least in the epitaxial devices fabricated in our lab—the reversal process starts with predominantly reverse domain nucleation at the bottom interface for the negative coercive field (thus when the polarization is switching from the downward to the upward direction)

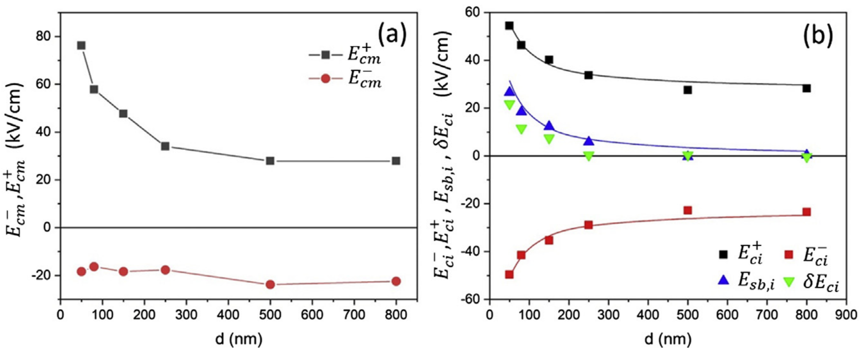

Figure 6.5 (A) Measured coercive field in the falling branch (E^-_{cm}) and rising branch (E^+_{cm}) of the PE-loop of capacitors as function of PZT thickness; (B) Extracted intrinsic coercive fields and self-bias field as function of thickness. The fits are according to Eqs. (6.14) and (6.16), respectively.

and at the top interface for the positive coercive field (switching from the upward to the downward direction) see Fig. 6.6.[4]

With this assumption one can write for the measured positive and negative coercive fields:

$$E^+_{cm}(d) = E^+_{ci}(d) + E_{sb,i}(d)$$
$$E^-_{cm}(d) = E^-_{ci}(d) + E_{sb,i}(d) \tag{6.6}$$

Here $E^+_{ci}(d)$ and $E^-_{ci}(d)$ are the (thickness dependent) intrinsic coercive fields of the top and bottom interfaces, respectively, and $E_{sb,i}(d)$ is an effective, intrinsic self-bias field present in the ferroelectric layer. Experimentally the measured self-bias field is usually defined from the measured coercive fields of the rising (E^+_{cm}) and falling (E^-_{cm}) branches of the hysteresis loop as:

$$E_{sb,m} = \left(E^+_{cm} + E^-_{cm}\right)/2 \tag{6.7}$$

Combining Eqs. (6.6) and (6.7) one has:

$$E_{sb,m}(d) = \left[E^+_{ci}(d) + E^-_{ci}(d)\right]/2 + E_{sb,i}(d) \tag{6.8}$$

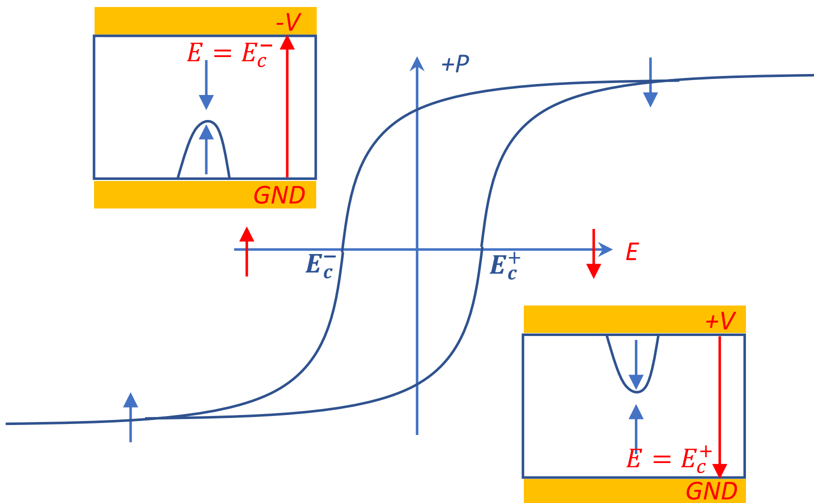

Figure 6.6 Schematic of reverse domain nucleation at positive and negative coercive fields. *Downward arrows* indicate top to bottom electrode direction.

[4] A systematic experimental proof of this assumption is still outstanding, however, the analysis of switching behavior in our devices is so far consistent with this interpretation.

and we find that the measured self-bias field contains a term $E_{sb,c} = \left(E_{ci}^{+} + E_{ci}^{-}\right)/2$ in addition to the intrinsic self-bias field $E_{sb,i}$. Hence $E_{sb,m}$ is only equal to $E_{sb,i}$ when $E_{ci}^{+} = -E_{ci}^{-}$. Since the polarization switching starts by reverse domain nucleation (predominantly) at one of the FE-electrode interfaces, one can see from cycling through the PE-loop, that nucleation starts at the top electrode for E_{ci}^{-} and at the bottom electrode for E_{ci}^{+}. Further one expects that the coercive fields depend on the interface properties, thus on (i) the electrode material, (ii) the quality of and the defects in the FE crystal structure near the interface and (iii) the interfacial roughness. Thus one can not a priori expect that $E_{ci}^{+} = -E_{ci}^{-}$.

From Fig. 6.5A it is seen that for large thicknesses, the coercive fields and therefore $E_{sb,m}$ are thickness independent. This suggests that one can describe the coercive field by a thickness independent term, $E_{ci}^{\pm}(\infty)$, and a term that goes to zero for large thicknesses, $\delta E_{ci}^{\pm}(d \to \infty) \to 0$. Since in our devices both electrodes are of the same material and the ferroelectric layer has at both sides the same crystalline quality, apart from a strain gradient at one side, one expects that for large thicknesses, one can write $E_{ci}^{+}(\infty) = -E_{ci}^{-}(\infty) + \Delta E_{ci}$. The term ΔE_{ci} accounts for a possible thickness-independent difference in (absolute) intrinsic coercive fields at both electrodes, which might be explained by a small difference in interfacial energies of the bottom and top electrode−ferroelectric interfaces. Different interfacial energies were shown to change the nucleation energy required for the creation of reverse domains and thus the coercive field (Tagantsev and Gerra, 2006). To make further analysis possible, it is now assumed that the thickness-dependent terms that contribute to the intrinsic coercive fields at both electrodes, have equal d-dependence, but opposite sign, $\delta E_{ci}^{-}(d) = -\delta E_{ci}^{+}(d)$. In Section 3.3, it is shown that this is the case for the model considered there. Thus one can write:

$$
\begin{aligned}
E_{cm}^{+}(d) &= \left[E_{ci}^{+}(\infty) + \delta E_{ci}^{+}(d)\right] + E_{sb,i}(d) \\
E_{cm}^{-}(d) &= \left[E_{ci}^{-}(\infty) - \delta E_{ci}^{+}(d)\right] + E_{sb,i}(d)
\end{aligned}
\tag{6.9}
$$

From the measured, thickness-dependent coercive field data, one can now extract the various parameters: from the opening of the loop for $d \to \infty$, and using $E_{sb,i}(d \to \infty) \to 0$, (which is the case for the model considered in Section 3.4), one finds:

$$E_{cm}^{+}(\infty) + E_{cm}^{-}(\infty) = E_{ci}^{+}(\infty) + E_{ci}^{-}(\infty) = \Delta E_{ci} \tag{6.10}$$

It also follows that for large film thicknesses, the intrinsic coercive fields are equal to the measured values, $E_{cm}^{+}(\infty) = E_{ci}^{+}(\infty)$, $E_{cm}^{-}(\infty) = E_{ci}^{-}(\infty)$. For finite d one finds, respectively, from the difference and the sum $E_{cm}^{+}(d) \mp E_{cm}^{-}(d)$ the relations:

$$\delta E_{ci}^{+}(d) = -\delta E_{ci}^{+}(d) = \left[E_{cm}^{+}(d) - E_{cm}^{-}(d) - E_{cm}^{+}(\infty) - E_{cm}^{-}(\infty)\right]/2 \tag{6.11}$$

$$E_{sb,i}(d) = \left[E_{cm}^{+}(d) + E_{cm}^{-}(d) - E_{cm}^{+}(\infty) - E_{cm}^{-}(\infty)\right]/2 \tag{6.12}$$

Thus one can calculate values for the thickness-dependent components of the intrinsic coercive fields and the self-bias field from the measured values, as shown in Fig. 6.5B.

Let us summarize the assumptions made to arrive at these results: (i) reversal by reverse domain nucleation at only one interface; (ii) a "symmetric" thickness dependence of the intrinsic coercive fields, $\delta E_{ci}^{\pm}(d)$, that goes to zero for $d \rightarrow \infty$; (iii) a (small) difference in the absolute intrinsic coercive fields, ΔE_{ci}, and (iv) an intrinsic self-bias field that goes to zero for large thicknesses, $E_{sb,i}(d)$.

From fitting the measured coercive fields, one finds $\Delta E_{ci} = 5$ kV/cm. Thus the (absolute value of the) intrinsic coercive field of the top electrode, $E_{ci}^{+}(\infty) = 28$ kV/cm, is slightly larger than that of the bottom electrode, $E_{ci}^{-}(\infty) = -23$ kV/cm. Further quantitative analysis is done after functional relations for $\delta E_{ci}^{\pm}(d)$ and $E_{sb,i}(d)$ have been obtained in the next sections.

Above we have extracted from the measurements the ferroelectric layer thickness dependence of the intrinsic coercive fields and the intrinsic self-bias field. The next task is to find explanations for the various thickness dependencies.

3.3 Thickness dependence of the coercive field

It has been observed already for a long time that the coercive field of thin film ferroelectric devices with all types of electrode materials scales approximately inversely with the FE-layer thickness (Dawber et al., 2003; Chandra et al., 2004). This scaling holds over many decades of electrode thickness. The explanation of this observation is that realistic electrode materials have a finite screening length λ because of a finite electron density of the electrode material. This causes incomplete charge compensation of the polarization charge at the FE-side of the interface. Assuming a simple exponential decay of the charge density in the electrode, one can model the effective screening charge as a delta distribution at a (screening) distance λ from the interface. Thus the polarization and screening charges are then effectively separated by a dielectric layer of thickness λ with the relative dielectric constant of the electrode material, ε_e, in the insulating state. In the early papers describing this explanation, no account was taken of the possibility of the presence of a dielectric layer at the electrode–ferroelectric interface. Here the effect of both screening layers and a dielectric layer is considered.

From Eqs. (6.1) and (6.2) one obtains (with the approximations $\lambda/\varepsilon_e d_{FE} \ll 1$, $E_i \approx P_s/\varepsilon_0\varepsilon_i$):

$$V = dE_m = d_{FE}E_{FE} + \frac{P_s}{\varepsilon_0}\left(\frac{d_i}{\varepsilon_i} + \frac{2\lambda}{\varepsilon_e}\right) \tag{6.13}$$

(when taking a self -bias field into account one should make the replacement $E_m \leftrightarrow E_m - E_{sb,i}(d)$). Taking the field value in the ferroelectric equal to that of the intrinsic coercive field E_{ci}, i.e., when stable reverse domains arise at the electrode interface, one finds that the measured coercive field is layer thickness dependent.

$$E_{cm}^{\pm}(d) = E_{ci}^{\pm}\left(1 + \frac{1}{d}\left[\frac{P_s}{\varepsilon_0 |E_{ci}^{\pm}|}\left(\frac{d_i}{\varepsilon_i} + \frac{2\lambda}{\varepsilon_e}\right) - d_i\right]\right) \tag{6.14}$$

Thus at large thicknesses, the measured coercive field is equal to the intrinsic field, $E_{cm}^{\pm}(\infty) = E_{ci}^{\pm}(\infty)$, whereas for small film thicknesses, the measured coercive field can become significantly larger than the intrinsic field.[5] Note that the above result corresponds to Eq. (6.9), after correction for an internal bias field, in the limit of small d_i as compared to the other term in the square brackets. From fitting the measured $E_{cm}^{+}(d)$ and $E_{cm}^{-}(d)$ values in Fig. 6.5A (solid curves) simultaneously one finds an effective length $\left(\frac{d_i}{\varepsilon_i} + \frac{2\lambda}{\varepsilon_e}\right) = 0.03$ Å .

The effective length value experimentally determined from the measured coercive fields is of the same order of magnitude as that found from the loop canting. However no explanation was found for the factor 3 difference.

3.4 Internal self-bias field due to trapped charge

An internal self-bias field can have several causes. First the case of an asymmetric charge distribution across the FE-layer is considered.[6] Consider the simple case of a sheet of positive charge σ at the interface of the near bottom electrode dielectric layer and the FE-layer, as shown in Fig. 6.1B. This is the simplification of a distribution of charge that might be present in the dielectric layer at the bottom electrode. Continuity of the displacement current shows that Eq. (6.1b) is changed to (with $\varepsilon_0 E_{FE} \ll P_z$):

$$E_i = \frac{P_z + \sigma}{\varepsilon_0 \varepsilon_i} \tag{6.15}$$

Eq. (6.13) becomes $V = dE_m = d_{FE}E_{FE} + \frac{P_s}{\varepsilon_0}\left(\frac{d_i}{\varepsilon_i} + \frac{2\lambda}{\varepsilon_e}\right) + \frac{\sigma}{\varepsilon_0}\left(\frac{d_i}{\varepsilon_i} + \frac{\lambda}{\varepsilon_e}\right)$. The measured voltage in the presence of the charge sheet, V_σ, is thus offset by the self-bias voltage $V_{sb,\sigma} = V_\sigma - V_{\sigma=0} = \frac{\sigma}{\varepsilon_0}\left(\frac{d_i}{\varepsilon_i} + \frac{\lambda}{\varepsilon_e}\right)$ and the P-E loop is shifted to the left for positive $V_{sb,\sigma}$, i.e., positive σ. The self-bias field scales inversely with the layer thickness as:

$$E_{sb,\sigma}(d) = \frac{V_{sb,\sigma}}{d} = \frac{\sigma}{\varepsilon_0 d}\left(\frac{d_i}{\varepsilon_i} + \frac{\lambda}{\varepsilon_e}\right) \tag{6.16}$$

[5] Taking the absolute value of the coercive field in the square bracketed term accounts for the inverted directions of the polarization for positive and negative coercive fields.

[6] Note that a homogenous charge distribution does not affect the polarization hysteresis loop.

It is easily shown that the self-bias field has the opposite sign in the case that the dielectric layer with the trapped charge layer is at the top electrode. Then the loop shifts to the right for positive trapped charge.

A second cause for self-bias is the use of top and bottom electrode materials with different work functions W (in Volt). Due to this difference, the Fermi-level in the ferroelectric layer is tilted, causing a build-in electric field that also scales inversely with the layer thickness, $E_{sb,W} = (W_t - W_b)/d$.[7]

The net intrinsic self-bias field is the sum of the different self-bias fields:

$$E_{sb,i}(d) = E_{sb,\sigma}(d) + E_{sb,W}(d) \tag{6.17}$$

In Fig. 6.5B the measured intrinsic self-bias field data as function of FE-layer thickness, $E_{sb,i}(d)$, has been fitted with Eq. (6.17).

At this point one can, on the basis of the experimental data, not yet distinguish between the different causes of the self-bias field. However for the devices considered here, the same electrode materials are used, therefore one may assume that $E_{sb,W}$ is small and in the following, it is assumed that the self-bias is dominated by the contribution of $E_{sb,\sigma}$. From the fitting and using the approximation $\left(\frac{d_i}{\varepsilon_i} + \frac{\lambda}{\varepsilon_e}\right) \approx \left(\frac{d_i}{\varepsilon_i} + \frac{2\lambda}{\varepsilon_e}\right) \approx O(0.1)$ Å, one finds an (effective) charge density of the order of $\sigma_{eff} = +0.12$ C/m^2. We have labeled this charge as effective since below it is shown that this charge may have multiple causes.

3.5 Charged dielectric layer caused by the flexoelectric effect

The above results are based on the assumptions of the presence of a charged, non-switching, dielectric layer at one of the electrodes and finite screening lengths in the electrodes. With these assumptions, we are able to describe the change of the slanting of the hysteresis loop, the change in self-bias, and the change of coercive field with varying thickness of the ferroelectric layer. The next question is how to explain the presence and properties of this dielectric layer at the bottom electrode. Here we follow closely the discussion in (Tagantsev and Gerra, 2006). Important hints are the TEM results of Fig. 6.2, showing line dislocations at approximately equal distances at the SRO/PZT bottom interface and the XRD analysis shown in Fig. 6.3. The misfit dislocations are spaced by about 12−13 nm. This corresponds well with the epitaxial misfit between the short axis lattice parameter of the PZT tetragonal unit cell of this composition, $a_{PZT} = 4.04$ Å, (and long axis lattice parameter $c_{PZT} = 4.11$ Å) and the substrate, $a_{STO} = 3.905$ Å.[8] The in-plane mismatch strain between PZT and SRO causes a compressive strain and growth of the PZT with the short axis in plane,

[7] In case the Fermi-level of one of the electrodes is pinned by defects at the FE-electrode interface, the self-bias field is determined by the pinning energy levels.

[8] As is well known for epitaxial growth of SRO on STO, the SRO bottom electrode layer is in general fully strained to the substrate, thus the in-plane lattice parameter of the SRO layer is equal to that of the substrate.

thus $\varepsilon_{ip} = (a_{STO} - a_{PZT})/a_{PZT} \approx 0.035$ in the PZT layer. This strain can be relaxed by line dislocations in the PZT, spaced by the interdislocation distance, that can be estimated as $l_{dl} \approx a_{STO}/|\varepsilon_{ip}| \approx 12$ nm. This value corresponds well with the observed spacing between the line defects. The line defects are the only defects observed at the interface and are therefore considered to be the cause of the strain relaxation in the PZT layer. The strain in the layer relaxes over a layer with a thickness of about l_{dl} to the average in-plane lattice parameter in the bulk of the film, a^*_{PZT}. Thus we can estimate the thickness of the strain relaxation layer as $d_i \approx l_{dl} = 12$ nm. If it is assumed that $2\lambda/\varepsilon_e \ll d_i/\varepsilon_i$, this results in an estimated value for the relative dielectric constant of the strained layer, $\varepsilon_i \approx 1200$.[9]

Although PZT(52/48) has a tetragonal unit cell, in clamped, thicker thin films ($\gg 100$ nm) one measures usually average lattice parameters, a^*_{PZT} and c^*_{PZT}. This is due to the nanodomain structure that is formed for this composition. The average values are somewhere in between the bulk values of the lattice parameters $a_{PZT} < a^*_{PZT} < c^*_{PZT} < c_{PZT}$ (Steenwelle, 2012).[10]

With this information one can explain and analyze the strain gradient layer. Over a distance l_{dl} the in-plane lattice parameter relaxes from the strained value a_{STO} to the effective relaxed value, a^*_{PZT}. This effective value can be determined from the XRD measurements of the effective out-of-plane lattice parameter c^*_{PZT}, assuming volume conservation of the PZT unit cell under strain, $(a^*_{PZT})^2 c^*_{PZT} \approx (a_{PZT})^2 c_{PZT} = V_{uc}$.The out-of-plane strain-gradient of the (equal) in-plane strains can thus be estimated as:

$$\frac{\partial \epsilon_{xx}}{\partial z}\left(=\frac{\partial \varepsilon_{yy}}{\partial z}\right) \approx \frac{\varepsilon_{xx}(0) - \varepsilon_{xx}(-l_{dl})}{l_{dl}} = \left(\frac{a_{STO} - a_{PZT}}{a_{PZT}} - \frac{a^*_{PZT} - a_{PZT}}{a_{PZT}}\right)/l_{dl}$$
$$= \left(\frac{a_{STO} - a^*_{PZT}}{a_{PZT}}\right)/l_{dl} \approx \frac{\varepsilon_{ip}|\varepsilon_{ip}|}{a_{STO}} \qquad (6.18)$$

In the last step we made the approximation $a^*_{PZT} \approx a_{PZT}$. ($z = 0$ corresponds to the bottom electrode–dielectric interface, $z = -l_{dl}$ is at the dielectric-ferroelectric interface. Positive z is directed downwards, corresponding to a positive field direction). Similarly the out-of-plane strain gradient is estimated as:

[9] With $\lambda_{SRO} = 0.07$ Å (Wang et al., 2020), the assumption is valid for $\varepsilon_e \gg 1.4$. Usual values for perovskites are $\varepsilon_e = 5..20$, hence this limit applies.

[10] For the compressively strained film discussed here, a^*_{PZT} and c^*_{PZT} correspond to the in-plane and out-of-plane lattice parameters of the film. a^*_{PZT} and c^*_{PZT} not only depend on the lattice thermal mismatch with the substrate but also on the a/c domain structure. In this composition, the domain sizes are so small, (i.e. of the size or smaller than the coherence length of the used X-ray beam of standard lab equipment) that the domain structure cannot be resolved and the obtained lattice parameters, in, for example, a $\theta - 2\theta$ scan, are an average of the lattice parameters of c- and a- oriented nano-sized domains in, for example, the in-plane direction.

$$\frac{\partial \varepsilon_{zz}}{\partial z} \approx \left(\frac{c^*_{PZT}(0) - c^*_{PZT}(-l_{dl})}{c_{PZT}}\right)/l_{dl} \approx \frac{\varepsilon_{op}|\varepsilon_{ip}|}{a_{STO}} \approx -\frac{2\varepsilon_{ip}|\varepsilon_{ip}|}{a_{STO}} \tag{6.19}$$

The value of $c^*_{PZT}(0)$ and the last step follow from volume conservation, while $c^*_{PZT}(-l_{dl})$ was determined experimentally. Note that ε_{ip} (here negative because compressive) and ε_{op} (here therefore positive) have opposite signs, therefore also the in-plane and out-of-plane strain gradients have opposite signs.

The presence of strain gradients indicates that the flexoelectric effect may play a role in the observed self-bias. Due to the strain gradients in the relaxation layer at the bottom interface, an effective electrical field in the downward direction is expected to be created in this layer, which can be quantified as:

$$E_{eff} = \phi_{11}\frac{\partial \varepsilon_{zz}}{\partial z} + \phi_{12}\left(\frac{\partial \varepsilon_{xx}}{\partial z} + \frac{\partial \varepsilon_{yy}}{\partial z}\right) \approx \phi_{eff}\frac{\varepsilon_{ip}|\varepsilon_{ip}|}{a_{STO}} \tag{6.20}$$

Here ϕ_{ij} are normalized (or flexocoupling) coefficients, which are related to the flexoelectric coefficients μ by $\phi = \mu/\chi$ (Zubko et al., 2013), with $\chi \approx \varepsilon_r$ the susceptibility. The flexocoupling coefficients were predicted to be of the order of $\phi = q/4\pi\varepsilon_0 a \approx 1-10$ V for simple ionic solids (Kogan, 1964). With for the perovskite a the interatomic spacing between the B-site ion and the O-ions, about 2 Å, and $q = 4e$ the B-ion charge, one finds $\phi_{eff} \approx 29$ V, which is of the same order as found experimentally for PZT, 25−72 V (Zubko et al., 2013). Thus for our case of compressive in-plane strain in the PZT at the interface, we find an upward-directed effective field in the strain relaxation layer of the order of a (few) MV/cm. This field is so large that the local polarization is pinned in the same direction as this effective field, or said otherwise the polarization becomes nonswitchable for all usually applied externally applied fields. Only for externally applied fields much larger than E_{eff} and oppositely oriented, the polarization vector in the strain relaxation layer can be switched.

Let us shortly dwell on the issue of the direction of the effective field. The unit cells in the strain relaxation layer can be assumed to have a trapezoidal shape, widening in the direction away from the substrate interface. One can picture that at the top side of the enclosed oxygen octahedron there is more space for the positively charged B-atom of the perovskite, thus one expects that the strain gradient enhances the upwards displacement of this ion. Hence the strain gradients create an upward-directed, fixed polarization, which can be associated with an upward-directed effective field. E_{eff}. The strain also increases this fixed polarization, P_M, to a value larger than the switchable saturation polarization P_s of the unstrained PZT due to the compressive strain, with a lower bound $P_M \geq P_s = 0.5$ C/m^2.

In conclusion, the model predicts that in the strain relaxation layer the polarization is pinned, hence the layer has become nonswitchable or passive. The strain gradient causes atomic displacements that can be translated in an upward directed effective field, E_{eff}. This field causes pinning of the polarization vector P_M in the direction of the upper electrode.

Now we have the ingredients to explain the self-bias in our devices. The displacement continuity across the interface of the strain-relaxation layer and the switchable ferroelectric layer, reads now:

$$\varepsilon_0 E_{FE} + P_z - \varepsilon_0 \varepsilon_i \left(E_i - E_{eff}\right) - P_M = \sigma \tag{6.21}$$

This leads to the self-bias field due to the flexoelectric effect and interfacial charge:

$$E_{sb,\,fe+\sigma} = \frac{d_i}{d}\left(\frac{P_M + \sigma}{\varepsilon_0 \varepsilon_i} + E_{eff}\right) = \frac{d_i \sigma_{eff}}{d \varepsilon_0 \varepsilon_i} \tag{6.22}$$

This defines in the last step the effective charge $\sigma_{\text{eff}} = P_M + \sigma + \varepsilon_0 \varepsilon_i E_{\text{eff}}$, already preluded upon above. Experimentally its value was estimated as $\sigma_{eff} = 0.12$ C/m^2. From the above astimates for P_M and E_{eff} one finds $P_M + \varepsilon_0 \varepsilon_i E_{eff} \approx -1.6$ C/m^2 (negative sign denotes a vector oriented toward the top electrode), so that a positive free charge density $\sigma = +1.7$ C/m^2 has to be assumed.

In general, the most probable free charges in the PZT are positively charged oxygen vacancies (OVs), OV^{2+}, and the negatively charged electrons, e^-. Since σ is positive one expects the presence of oxygen vacancies with a density ρ_{OV} in the relaxation layer. Its value can be estimated from the interfacial layer charge density by assuming an exponentially decaying OV density as $\rho_{OV} = \sigma/2ed_i = 0.03$ OV per unit cell volume or an average OV-density in the strain relaxation layer of 0.5%. This is considered a plausible OV concentration, which is expected to arise during the growth under compressive epitaxial strain of the strain relaxation layer.

4. Discussion and conclusions

Above it is shown that several trends with respect to the polarization loop as function of thickness of the ferroelectric layer, i.e., the slanting of the loop, the value, and sign of the coercive field and the self-bias field, can be explained by the presence of a positively charged, dielectric layer at the bottom electrode−ferroelectric interface. Such a layer in turn can be explained by the observed compressive strain gradient layer in the ferroelectric at this interface. A strain relaxation layer can cause a nonswitching, thus dielectric, layer through the flexoelectric effect. To explain the observed self-bias field, one has to assume in addition that this layer is positively charged. OVs are the most likely candidate for these charges, which one would expect to be present because these also present a mechanism for the strain relaxation.

So far the model does not allow the separation of the effects of the dielectric interfacial layer and the presence of possible screening layers in the investigated SRO/PZT/SRO-on-STO devices. This would require the use of devices with electrodes with different screening lengths.

It is noted that in our lab, the above-observed effects are very clear in SRO/PZT/SRO-on-STO devices. However, we have no indications for the presence of similar

effects in symmetric devices grown with different electrode materials (Pt or $LaNiO_3$), or grown on Si substrates. This is attributed to the observation that STEM analysis of the different interfaces indicate that only on STO/SRO the PZT grows epitaxially with a low density of interfacial defects, allowing for the presence of a relatively thick strain relaxation layer at this interface. In the other cases, the defect density appears to be so large that no strain gradient can develop. Consequently there can be little to no flexoelectric effect and therefore no (thick) non-switchable dielectric layer present.

It is noted that the charge in the interfacial layer appears to be changed by a long positive or negative constant field bias or by field cycling (Boota et al., 2016), as shows up in a change of the self-bias field, reflecting the mobility of charged species as OV's and electrons, changing the effective charge in the interfacial layer.

References

Auciello, O., Paz de Araujo, C.A., Celinska, J., 2014. Review of the Science and Technology for Low- and High-Density Nonvolatile Ferroelectric Memories, Emerging Non-volatile Memories, vol. 3. Springer.

Boota, M., Houwman, E.P., Dekkers, M., Nguyen, M., Rijnders, G., 2014. Epitaxial $Pb\left(Mg_{1/3}Nb_{2/3}\right)O_3 - PbTiO_3\ (67/33)$ thin films with large tunable self-bias field controlled by a $PbZr_{1-x}Ti_xO_3$ interfacial layer. Appl. Phys. Lett. 104, 182909.

Boota, M., Houwman, E.P., Dekkers, M., Nguyen, M.D., Vergeer, K.H., Lanzara, G., Koster, G., Rijnders, G., 2016. Properties of epitaxial, (001)- and (110)-oriented $\left(Pb\left(Mg_{1/3}Nb_{2/3}\right)O_3\right)_{2/3} - (PbTiO_3)_{1/3}$ films on silicon described by polarization rotation. Sci. Technol. Adv. Mater. 17, 45.

Chandra, P., Dawber, M., Littlewood, P.B., Scott, J.F., 2004. Ferroelectrics 313, 7.

Dawber, M., Chandra, P., Littlewood, P.B., Scott, J.F., 2003. J. Phys. Condens. Matter 15, L393.

Dekkers, M., Nguyen, M.D., Steenwelle, R., te Riele, P.M., Blank, D.H.A., Rijnders, G., 2009. Ferroelectric properties of epitaxial $Pb(Zr,Ti)O_3$ thin films on silicon by control of crystal orientation. Appl. Phys. Lett. 95, 012902.

Do, M.-T., 2021. Mechanisms of Polarization Fatigue in Ferroelectric PbZr0:52Ti0:48O3 Epitaxial Thin-Film Capacitors (Ph.D. thesis). University of Twente.

Do, M.T., et al., 2020. Interfacial dielectric layer as an origin of polarization fatigue in ferroelectric capacitors. Sci. Rep. 10, 7310.

Do, M.T., Gauquelin, N., Nguyen, M.D., Blom, F., Verbeeck, J., Koster, G., Houwman, E.P., Rijnders, G., 2021. Interface degradation and field screening mechanism behind bipolar-cycling fatigue in ferroelectric capacitor. APL Mater. 9, 021113.

Eom, C.-B., Trolier-McKinstry, S., 2012. MRS Bull. 37, 1007.

Funakubo, H., Dekkers, M., Sambri, A., Gariglio, S., Shklyarevskiy, I., Rijnders, G., 2012. MRS Bull. 37, 1030.

Garcia, V., Bibes, M., 2014. Ferroelectric tunnel junctions for information storage and processing. Nat. Commun. 5, 4289.

Isarakorn, D., Sambri, A., Janphuang, P., Briand, D., Gariglio, S., Triscone, J.-M., Guy, F., Reiner, J.W., Ahn, C.H., de Rooij, N.F., 2010. J. Micromech. Microeng. 20, 055008.

Ishiwara, H., 2012. Ferroelectric random access memories. J. Nanosci. Nanotechnol. 12, 7619.

Kim, D.J., Lu, H., Ryu, S., Bark, C.-W., Eom, C.-B., Tsymbal, E.Y., Gruverman, A., 2012. Ferroelectric tunnel memristor. Nano Lett. 12, 5697.

Kogan, S.M., 1964. Piezoelectric effect during inhomogeneous deformation and acoustic scattering of carriers in crystals. Sov. Phys. Solid State 5, 2069.

Koh, H.H., Kobayashi, T., Lee, C., 2011. Opt. Express 19, 13812.

Li, L., Liao, Z., Gauquelin, N., Nguyen, M.D., Hueting, R.J.E., Gravesteijn, D.J., Lobato, I., Houwman, E.P., Lazar, S., Verbeeck, J., Koster, G., Rijnders, G., 2018. Epitaxial stress-free growth of high crystallinity ferroelectric $PbZr_{0.52}Ti_{0.48}O_3$ on GaN/AlGaN/Si(111) substrate. Adv. Mater. Interfaces 5, 1700921.

Li, L., Liao, Z., Nguyen, M.D., Hueting, R.J.E., Gravesteijn, D.J., Houwman, E.P., Rijnders, G., Koster, G., 2020. Epitaxial growth of full range of compositions of (1 1 1) $PbZr_{1-x}Ti_xO_3$ on GaN. J. Cryst. Growth 538, 125620.

Lou, X.J., Zhang, M., Redfern, S.A.T., Scott, J.F., 2006. Local phase decomposition as a cause of polarization fatigue in ferroelectric thin films. Phys. Rev. Lett. 97, 177601.

Lou, X.J., Zhang, M., Redfern, S.A.T., Scott, J.F., 2007. Fatigue as a local phase decomposition: a switching-induced charge-injection model. Phys. Rev. B75, 224104.

Lou, X.J., 2009. Polarization fatigue in ferroelectric thin films and related materials. J. Appl. Phys. 105, 024101.

Ma, C., Luo, Z., Huang, W., Zhao, L., Chen, Q., Lin, Y., Liu, X., Chen, Z., Liu, C., Sun, H., Jin, X., Yin, Y., 2020. Sub-nanosecond memristor based on ferroelectric tunnel junction. Nat. Commun. 11, 1439.

Mikheev, V., Chouprik, A., Lebedinskii, Y., Zarubin, S., Markeev, A.M., Zenkevich, A.V., Negrov, D., 2020. Memristor with a ferroelectric HfO_2 layer: in which case it is a ferroelectric tunnel junction. Nanotechnology 31, 215205.

Nematollahi, M., Lucke, P., Bayraktar, M., Yakshin, A., Rijnders, A.J.H.M., Bijkerk, F., 2019. Nanoscale piezoelectric surface modulation for adaptive extreme ultraviolet and soft X-ray optics. Opt. Lett. 44, 5104.

Nguyen, M.D., Dekkers, M., Houwman, E., Steenwelle, R., Wan, X., Roelofs, A., Schmitz-Kempen, T., Rijnders, G., 2011. Misfit strain dependence of ferroelectric and piezoelectric properties of clamped (001) epitaxial $PbZr_{0.52}Ti_{0.48}O_3$ thin films. Appl. Phys. Lett. 99, 252904.

Nguyen, M.D., Trinha, T.Q., Dekkers, M., Houwman, E.P., Vu, H.N., Rijnders, G., 2014. Effect of dopants on ferroelectric and piezoelectric properties of lead zirconate titanate thin films on Si substrates. Ceram. Int. 40, 1013−1018.

Nguyen, M.D., Yuan, H., Houwman, E.P., Dekkers, M., Koster, G., ten Elshof, J.E., Rijnders, G., 2016a. ACS Appl. Mater. Interfaces 8, 31120.

Nguyen, M.D., Dekkers, M., Houwman, E.P., Vu, H.T., Vu, H.N., Rijnders, G., 2016b. Lead-free $(K_{0.5}Na_{0.5})NbO_3$ thin films by pulsed laser deposition driving MEMS-based piezoelectric cantilevers. Mater. Lett. 164, 413.

Nguyen, M.D., Houwman, E.P., Dekkers, M., Rijnders, G., 2017a. ACS Appl. Mater. Interfaces 9, 9849.

Nguyen, M., Houwman, E., Dekkers, M., Schlom, D., Rijnders, G., 2017b. APL Mater 5, 074201.

Nguyen, M.D., Houwman, E.P., Yuan, H., Wylie-van Eerd, B.J., Dekkers, M., Koster, G., ten Elshof, J.E., Rijnders, G., 2017c. Controlling piezoelectric responses in $PbZr_{0.52}Ti_{0.48}O_3$ films through deposition conditions and nanosheet buffer layers on glass. ACS Appl. Mater. Interfaces 9, 35947.

Priya, S., et al., 2017. A review on piezoelectric energy harvesting: materials, methods, and circuits. In: Energy Harvesting and Systems, vol. 4. De Gruyter.

Setter, N., Damjanovic, D., 2006. Ferroelectric thin films: review of materials, properties, and applications. J. Appl. Phys. 100, 051606.

Steenwelle, R., 2012. PhD-thesis. University of Twente.

Tadigadapa, S., Mateti, K., 2009. Meas. Sci. Technol. 20, 092001.

Tagantsev, A.K., Gerra, G., 2006. Interface-induced phenomena in polarization response of ferroelectric thin films. J. Appl. Phys. 100, 051607.

Vu, H.T., Nguyen, M.D., Houwman, E.P., Boota, M., Dekkers, M., Vu, H.N., Rijnders, G., 2015. Mater. Res. Bull. 72, 160.

Wang, J., Nguyen, M.D., Gauquelin, N., Verbeeck, J., Do, M.T., Koster, G., Rijnders, G., Houwman, E.P., 2020. On the importance of the work function and electron carrier density of oxide electrodes for the functional properties of ferroelectric capacitors. Phys. Status Solidi RRL 1900520.

Wen, Z., Wu, D., 2020. Ferroelectric tunnel junctions: modulations on the potential barrier. Adv. Mater. 32, 1904123.

Zubko, P., Catalan, G., Tagantsev, A.K., 2013. Flexoelectric effect in solids. Annu. Rev. Mater. Res. 43, 387.